Ultralow lattice thermal conductivity in quasi-one-dimensional BiI_3 with suppressed phonon coherence

Chenxin Zhang,[1] Jie Sun,[2] Jiewei Cheng,[1] and Qian Wang[1,*]

[1]*School of Materials Science and Engineering, Peking University, Beijing 100871, China*

[2]*Institute of Engineering Innovation, Graduate School of Engineering, University of Tokyo, Bunkyo-ku, Tokyo 113-0032, Japan*

(Received 3 August 2024; revised 31 October 2024; accepted 5 November 2024; published 25 November 2024)

The enhanced coherence thermal transport in complex materials poses challenges in achieving ultralow lattice thermal conductivity in crystalline materials. In this work, based on a global structure search, we find a stable quasi-one-dimensional crystal, q-1D BiI_3, with a simple unit cell containing eight atoms. Using the Wigner thermal transport theory and machine-learning potential, we derive Pearson correlation coefficient matrices based on the calculations of over one million coherent modes, and find that the phonon coherent thermal conductivity is mainly correlated with the generalized group velocity, the frequency interval of coherent phonon modes, and the generalized coherent lifetime. Especially, the unique geometry and hierarchical bonding features of q-1D BiI_3 induce significant anharmonicity, while the small number of atoms in the unit cell reduces the Wigner time limit for the wavelike tunneling of phonons, suppressing the coherence thermal transport. Thus, the synergistic effect of enhanced phonon scattering and reduced phonon coherence leads to an ultralow lattice thermal conductivity of 0.088 (0.099) $W\,m^{-1}\,K^{-1}$ in the $x(y)$ direction. Our work demonstrates the significance of suppressing phonon coherence for achieving ultralow lattice thermal conductivity of crystal materials.

DOI: 10.1103/PhysRevB.110.174309

I. INTRODUCTION

Developing new materials with ultralow thermal conductivity is of great significance for thermoelectric conversion, energy storage technologies, and thermal insulation in micro and nano electronic devices [1,2]. In recent years, significant progress has been made in the study of crystalline materials with low thermal conductivity based on Boltzmann transport theory [3] and Slack's rule [4]. For instance, layered $Bi_4O_4SeCl_2$ was found to exhibit an ultralow cross-plane thermal conductivity of 0.17 $W\,m^{-1}\,K^{-1}$ owing to its complex structure and high average atomic weight [5,6]. As an outstanding thermoelectric material, Ag_8SnSe_6 has a lattice thermal conductivity lower than 0.50 $W\,m^{-1}\,K^{-1}$ due to the weak interatomic bonding [7]. Meanwhile, advances have also been made in thermal transport theories, driven by the exploration of ultralow thermal conductivity of materials. A two-channel model was suggested for crystals with ultralow thermal conductivity based on the study of Tl_3VSe_4 [8]. In 2019, Simoncelli *et al.* proposed a unified theory of thermal transport in crystals and glasses [9], and further developed the Wigner formulation of thermal transport in solids in 2022 [10] for providing more accurate description of the lattice thermal conductivity of strongly anharmonic crystals with complex structures.

It has been found that it is difficult to follow Slack's rule [4] for achieving ultralow lattice thermal conductivity in systems with complex structures, weak atomic bonding, large average atomic mass, and strong anharmonicity. For instance, the lattice thermal conductivity of many complex materials composed of clusters as the building units is in the range 0.21−5.34 $W\,m^{-1}\,K^{-1}$ [11,12]. The recently reported $Pt_3Bi_4Q_9$ (Q = S, Se) systems have low lattice thermal conductivities ranging 0.59−0.81 $W\,m^{-1}\,K^{-1}$ at room temperature [13]. Although an extremely low cross-plane thermal conductivity of 0.05 $W\,m^{-1}\,K^{-1}$ was found in the disordered WSe_2 thin film, the corresponding value of single-crystal WSe_2 is about 30 times higher than that of the disordered film [14]. Very recently, an ultralow lattice thermal conductivity of 0.25 $W\,m^{-1}\,K^{-1}$ in $AgTlI_2$ single crystal was reported [15], demonstrating the possibility of achieving ultralow thermal conductivity in anharmonic crystals with a simple lattice structure by further suppressing both phonon propagation and coherence effects, which motivates us to carry out this work by considering three key factors: heavy element, strong anharmonicity, and weak phonon coherence.

In this work, starting from searching for new structures composed of heavy elements of Bi and I, a different quasi-1D crystal phase of BiI_3 (q-1D BiI_3) is found, which has similar geometry to the experimentally synthesized q-1D TiS_3 with a simple unit cell and intrinsically strong anharmonicity [16–18]. We investigate its lattice thermal transport based on the Wigner thermal transport theory and the neuroevolution potential (NEP) [19] with a focus on the coherent thermal conductivity. We also study other related properties, including the generalized description of the velocity and lifetime of coherent phonon modes, as well as the complexity of phonon dispersion to demonstrate the strategy for designing materials with ultralow thermal conductivity, and to elucidate the physical mechanism of how strongly anharmonic simple crystal structures synergistically regulate the

*Contact author: qianwang2@pku.edu.cn

two-channel phonon thermal transport to achieve ultralow thermal conductivity.

II. COMPUTATIONAL METHODS

A. First-principles calculations

Our calculations are carried out based on density functional theory (DFT) and the projector-augmented wave method (PAW) [20,21] implemented in the Vienna *ab initio* simulation package (VASP) [22]. The electronic exchange-correlation interaction is treated by using the Perdew-Burke-Ernzerhof functional (PBE) [23] within the generalized gradient approximation (GGA) [24]. The DFT-D3 functional is applied for describing the interactions between BiI_3 chains [25]. The kinetic energy cutoff for wave function is set to 550 eV. The Brillouin zone is represented with the Monkhorst-Pack [26] grid of $10 \times 6 \times 15$ **k** point for geometry optimization, while the convergence criteria for energy and force are set as 10^{-8} eV and 10^{-6} eV/Å, respectively. A $3 \times 2 \times 4$ supercell of q-1D BiI_3 and the canonical ensemble (*NVT*) are used for our *ab initio* molecular dynamics (AIMD) simulations.

B. Wigner thermal transport

The calculation of thermal conductivity is based on the Winger framework of lattice thermal transport [9,10]. the total lattice thermal conductivity κ_L is divided into the particlelike contribution (κ_L^P) and the coherence contribution (κ_L^C):

$$\kappa_L = \kappa_L^P + \kappa_L^C. \tag{1}$$

The lattice thermal conductivity and phonon properties are calculated using ShengBTE package [27]. The calculations of κ_L^C are conducted using our in-house codes within the Wigner framework [9,10]:

$$\kappa_L^{C,\alpha\beta} = \frac{\hbar^2}{k_B T^2 \Omega N} \sum_{\mathbf{q}} \sum_{i \neq j} \frac{\omega(\mathbf{q})_i + \omega(\mathbf{q})_j}{2} V^{\alpha}(\mathbf{q})_{ij} V^{\beta}(\mathbf{q})_{ji} \times \frac{\omega(\mathbf{q})_i \bar{N}(\mathbf{q})_i [\bar{N}(\mathbf{q})_i + 1] + \omega(\mathbf{q})_j \bar{N}(\mathbf{q})_j [\bar{N}(\mathbf{q})_j + 1]}{4[\omega(\mathbf{q})_i - \omega(\mathbf{q})_j]^2 + [\Gamma(\mathbf{q})_i + \Gamma(\mathbf{q})_j]^2} \times [\Gamma(\mathbf{q})_i + \Gamma(\mathbf{q})_j], \tag{2}$$

where α and β are the directions of the Cartesian coordinate system, $\hbar$, k_B, T, N, and Ω are the reduced Plank constant, Boltzmann constant, temperature, number of phonon wave vectors, and lattice volume, respectively, $\omega(\mathbf{q})_i$ and $\bar{N}(\mathbf{q})_i$ are the angular frequencies and the equilibrium Bose-Einstein distribution, indexed by wave vector $\mathbf{q}$ with the branch i, respectively, and $\Gamma(\mathbf{q})_i = 1/\tau(\mathbf{q})_i$ is the phonon linewidth (scattering rate) of each phonon; $V(\mathbf{q})_{ij}$ represents the generalized velocity matrix along different directions [see the Supplemental Material (SM) for details] [28]. The inputs for calculating κ_L^P are harmonic (second-order) and anharmonic (third- and fourth-order) interatomic force constants (IFCs). The phonon dispersions and eigenvectors are calculated via the PHONOPY code [31]. A $3 \times 3 \times 3$ **k** point grid is applied. One hundred perturbative structures for the calculation of anharmonic IFCs are generated using the Monte Carlo modified rattle procedure implemented in the HIPHIVE package [32]. The phonon spectra of q-1D BiI_3 under finite temperatures are calculated by using the self-consistent phonon theory implemented in HIPHIVE [32,33] with a perturbation approach based on anharmonic force constants up to the fourth order. A $4 \times 3 \times 5$ supercell is used for calculating second-order IFCs under finite temperatures. The cutoff distances for second-, third-, and fourth-order IFCs are set as 8.00, 7.30, and 6.30 Å for q-1D BiI_3, respectively (see Fig. S1 in the SM for details [28]). In ShengBTE calculations, the convergent **q** point grid of $7 \times 5 \times 9$ and a Gaussian scalebroad of 1.00 are used (see Fig. S2 in the SM [28]).

C. Neuroevolution potential

To speed up the calculation with high accuracy, we use the machine-learning potential, i.e., neuroevolution potential (NEP) developed by Fan *et al.* [34] to capture interatomic interactions for q-1D BiI_3. We have performed multiple AIMD calculations for a $3 \times 2 \times 4$ supercell of q-1D BiI_3 at temperatures ranging 200–900 K. Each calculation lasts for about 5–10 ps with a time step of 1 fs, where the initial 1 ps is taken for the lattice relaxation time. By sampling every 20 to 50 frames from the entire simulated trajectory, we obtain a total of 660 structures extracted as input configurations for the training data set. These selected structures are subjected to our DFT calculations using a $3 \times 3 \times 3$ **k** point grid to obtain energy and interatomic force information for training. The radial and angular cutoffs are set to 8.00 and 5.00 Å, respectively, while the rest are kept at default settings, and 10^6 steps are trained (see Note 2 and Fig. S3 in the SM [28]).

D. Homogeneous nonequilibrium molecular dynamics

To verify the accuracy of calculations within the Wigner framework, we further carry out the homogeneous nonequilibrium molecular dynamics (HNEMD) simulations employing the NEP and using the Graphics Processing Units Molecular Dynamics (GPUMD) package [34,35]. To avoid the influence of size effects in MD simulations, we use a $7 \times 5 \times 9$ supercell with 2520 atoms for thermal conductivity calculations. The structures are first relaxed using the isothermal-isobaric ensemble (*NPT*) for 100 ps, and then six independent HNEMD simulations are performed in the *NVT* with a duration of 10 ns at 300 K with a time step of 1 fs, taking the average as the final result (see Fig. S4 in the SM [28]).

III. RESULTS AND DISCUSSION

A. Geometric structure and stability

Motivated by previous studies on Bi_xI_{1-x} and the changes of their geometric structures under high pressure [36,37], we screen the geometric morphology of BiI_3 at 10 GPa by using the MAGUS software [38,39] combined with the machine learning potential in MLIP-2 [40] where the chemical element ratio is selected by comparing the formation enthalpy (ΔH) of Bi_xI_{1-x} in the Materials Project database [41] (see Note 3 and Fig. S5 in the SM [28]). Among the generated structures, the TiS_3-type q-1D BiI_3 structure is identified, as shown in Figs. 1(a) and 1(b), where the unit cell contains two Bi and six I atoms. The optimized structure possesses a monoclinic lattice with the symmetry of $P21/m$ (no. 11) and lattice parameters of $a = 8.22$ Å, $b = 10.00$ Å, $c = 4.14$ Å, and $\gamma = 102.04^\circ$ (Table SI in the SM). According to the convex hull of Bi_xI_{1-x} structures, we find that q-1D BiI_3 is

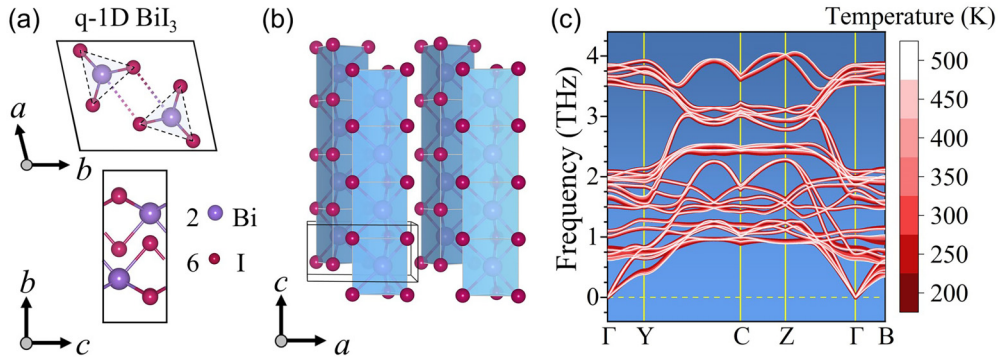

FIG. 1. Geometric structure and dynamical stability of q-1D BiI_3. (a) Top and side views of the unit cell, and (b) perspective view of the crystal structure of q-1D BiI_3. (c) Phonon spectra of q-1D BiI_3 within the temperature range 200–500 K.

a metastable phase of bismuth triiodides, but has a potential to be synthesized from the ground state $R-3$ BiI_3 [42] (see Figs. S5 and S6 in the SM [28]). We then calculate the phonon spectra of q-1D BiI_3 at the temperatures ranging 200–500 K. The results are plotted in Fig. 1(c), which shows no imaginary frequencies in their entire Brillouin zone, confirming that q-1D BiI_3 is dynamically stable at finite temperatures. The phonon spectrum at zero temperature is presented in Fig. S7(a) in the SM [28]. To confirm its mechanical stability, we calculate the stiffness tensor components C_{ij} (i, j ranging 1–6) using the Calorine package with our NEP for q-1D BiI_3 [34,35]. As a monoclinic lattice, all C_{ij} components possess independent values. We find that all the calculated eigenvalues of the stiffness tensor matrix are positive, satisfying the Born-Huang criteria [43], and indicating that q-1D BiI_3 is mechanically stable (see Note 5 in the SM for details). We have also verified the thermal stability of the q-1D BiI_3 structure by performing *ab initio* molecular dynamics (AIMD) simulations [see Fig. S7(b) in the SM [28]], and found that this structure can be stable at high temperature of 700 K.

B. Lattice thermal conductivities

We first calculate the electronic band structure of q-1D BiI_3 to verify the feasibility of analyzing its thermal transport properties only including phonon contributions. q-1D BiI_3 is found to possess semiconducting features with an indirect band gap of 1.93 eV (Fig. S8). Therefore, the thermal conductivity contributed from electrons can be neglected. We then calculate the lattice thermal conductivity of q-1D BiI_3 within the Wigner framework [28] by taking into account the contributions from both phonon scattering and phonon coherence. In all the relevant calculations, four-phonon scattering [44] is included. For comparison, calculations are also carried out for the light-element counterpart q-1D TiS_3 and the more complex $R-3$ BiI_3 that contains 24 atoms per unit cell. The calculated lattice thermal conductivities along the different directions for the three structures at different temperatures are plotted in Fig. 2(a). One can see that, for q-1D BiI_3, the intrachain thermal conductivity κ_L^z in the z direction is higher than the interchain thermal conductivity κ_L^x in the x direction, exhibiting strong anisotropy. The κ_L^z at 300 K is 0.61 $W\,m^{-1}\,K^{-1}$ including a phonon coherence contribution ($\kappa_L^{C,z}$) of 0.13 $W\,m^{-1}\,K^{-1}$, while the κ_L^x is only 0.088 $W\,m^{-1}\,K^{-1}$, including a $\kappa_L^{C,x}$ of 0.046 $W\,m^{-1}\,K^{-1}$. Compared to the thermal conductivities of q-1D BiI_3, q-1D TiS_3 possesses much higher κ_L^x (4.71 $W\,m^{-1}\,K^{-1}$) and κ_L^z (7.49 $W\,m^{-1}\,K^{-1}$) at 300 K, including larger contributions from phonon coherence $\kappa_L^{C,x}$ (0.16 $W\,m^{-1}\,K^{-1}$) and $\kappa_L^{C,z}$ (0.31 $W\,m^{-1}\,K^{-1}$). For the layered $R-3$ BiI_3 phase, both the interlayered lattice thermal conductivity κ_L^z (0.46 $W\,m^{-1}\,K^{-1}$) and the coherent portion $\kappa_L^{C,z}$ (0.26 $W\,m^{-1}\,K^{-1}$) are also found to be higher than the corresponding interchain values of q-1D BiI_3. Furthermore, to ensure the reliability of our computational results, we conduct the homogeneous nonequilibrium molecular dynamics (HNEMD) simulations for the κ_L^x of q-1D BiI_3 at 300 K, and find that the average simulation result of 0.088 $W\,m^{-1}\,K^{-1}$ matches well with that obtained based on the Wigner thermal transport theory calculations.

To understand the extremely weak particlelike phonon transport in q-1D BiI_3, we then calculate the phonon group velocities (V_i) and Grüneisen parameters (γ) of these three systems, and find that q-1D BiI_3 has lower V_i and larger γ than those q-1D TiS_3 and $R-3$ BiI_3, blocking the particlelike propagation of phonons (Figs. S9 and S10 in the SM [28]), resulting in a significantly lower particlelike contribution (κ_L^P).

We then conduct the correlation analysis of typical physical quantities that are closely related to phonon coherence in order to explore the physical mechanisms of the ultralow coherent thermal conductivity (κ_L^C). Due to the complexity induced by the coupling of coherent phonon modes, the difficulty of analyzing phonon properties is significantly increased compared to the phonon gas model that only considers individual phonon modes. Although our previous studies [45,46] showed that the frequency interval and linewidth of coherent phonon modes have a significant impact on coherent thermal transport properties in crystals, the correlations among various physical quantities remain unclear, which limits the accurate assessment of the contribution from phonon coherence to thermal transport in anharmonic crystals. To overcome this dilemma, we calculate the Pearson correlation coefficient matrices of the κ_L^C with the five main physical quantities, including the square of the generalized group velocity ($V_{ij}^2 = |V_{ij}V_{ji}|$), the frequency interval of coherent phonon modes ($\Delta\omega = |\omega_i - \omega_j|$), sum of linewidths (sumΓ=$\Gamma_i + \Gamma_j$), generalized coherent lifetime (τ_{ij}), and isochoric heat capacity of

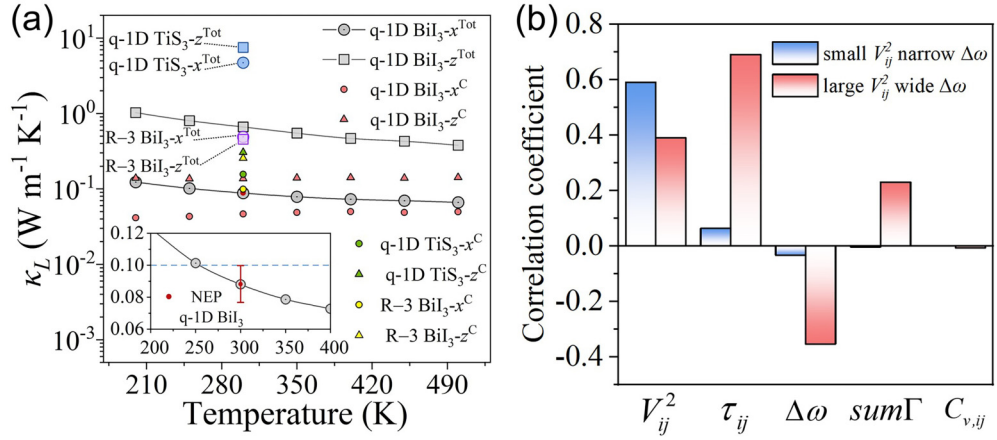

FIG. 2. Correlation analysis for the lattice thermal transport properties. (a) Calculated total lattice thermal conductivity and coherent thermal conductivity as a function of temperature (red dot with error bar for the HNEMD results). (b) Average Pearson correlation coefficients for the coherent thermal conductivity (κ_L^C), square of the generalized group velocity (V_{ij}^2), generalized coherent lifetime (τ_{ij}), frequency interval of coherent phonon modes ($\Delta\omega$), sum of linewidths (sumΓ), and isochoric heat capacity of coherent modes ($C_{v,ij}$) of q-1D BiI_3, $R-3$ BiI_3, and q-1D TiS_3.

coherent modes ($C_{v,ij}$), for describing phonon coherent behaviors via over one million calculated coherent modes within the Wigner framework. Due to the complex numerical distribution, it is very difficult to establish the relationship between the selected physical quantities through a direct comparison of the correlation across the entire parameter range. We found that the main contribution to κ_L^C comes from the coherent phonon modes with relatively small V_{ij}^2 and narrow $\Delta\omega$ (see Fig. S11 in the SM [28]), therefore we respectively calculated the correlation coefficients between the parameters for coherent phonon modes with V_{ij}^2 less than 10% of the maximum value ($V_{ij}^{2,\max}$) and $\Delta\omega/2\pi$ less than 0.5 THz. Calculations are also performed for $V_{ij}^2 > 0.1V_{ij}^{2,\max}$ and $\Delta\omega/2\pi > 0.5$ THz, as shown in Fig. S12 in the SM [28]. The calculated average results for the Pearson correlation coefficients are presented in Fig. 2(b), indicating the degree of importance of each parameter. One can see that in all the systems, when $V_{ij}^2 < 0.1V_{ij}^{2,\max}$ and $\Delta\omega/2\pi < 0.5$ THz, there is a clear correction between κ_L^C and V_{ij}^2, while the correlations with other parameters are not obvious. On the other hand, V_{ij}^2, τ_{ij}, and $\Delta\omega$ show a certain degree of correlation with κ_L^C, when $V_{ij}^2 > 0.1V_{ij}^{2,\max}$ and $\Delta\omega/2\pi > 0.5$ THz. Meanwhile, the importance of τ_{ij} and $\Delta\omega$ has significantly increased. Therefore, we further discuss the contribution of the three parameters, namely, V_{ij}^2, $\Delta\omega$, and τ_{ij}, suppressing coherent thermal conductivity in the simple crystal structure of q-1D BiI_3.

C. Generalized group velocity

To investigate the impact of the V_{ij}^2 on the coherent thermal conductivity, we respectively plot the projection of V_{ij}^2 in the x and z directions of q-1D BiI_3 in Figs. 3(a) and 3(b), as well as that in the x direction of q-1D TiS_3 in Fig. 3(c) for comparison. One can see that the V_{ij}^2 in the x direction of q-1D BiI_3 is significantly smaller than that of the z direction, while the V_{ij}^2 in the z direction of q-1D BiI_3 and in the x direction of q-1D TiS_3 exhibit similar magnitudes. Based on the Allen-Feldman model [47,48], the mode diffusivity (D_i) has a strong dependence on the V_{ij}^2:

$$D^\alpha(\mathbf{q})_i = \frac{\pi}{3\omega(\mathbf{q})_i^2}\sum_{i\neq j}\left|V^{\mathrm{AA},\alpha}(\mathbf{q})_{ij}\frac{\omega(\mathbf{q})_i+\omega(\mathbf{q})_j}{2}\right|^2 \cdot \delta[\omega(\mathbf{q})_i-\omega(\mathbf{q})_j], \tag{3}$$

$$V^{\mathrm{AA},\alpha}(\mathbf{q})_{ij} = \frac{\omega(\mathbf{q})_i+\omega(\mathbf{q})_j}{2\sqrt{\omega(\mathbf{q})_i\omega(\mathbf{q})_j}}V^\alpha(\mathbf{q})_{ij}, \tag{4}$$

where $V^{\mathrm{AA},\alpha}(\mathbf{q})_{ij}$ is the velocity operator defined by Auerbach and Allen and $\delta[\omega(\mathbf{q})_i-\omega(\mathbf{q})_j]$ is the Dirac Delta function that can be approximated using Lorentzian broadening of width greater than the average mode frequency interval ($\Delta\omega_{\mathrm{ave}}$) [49]. As shown in Fig. S10 in the SM [28], the values of D_i for q-1D TiS_3 and $R-3$ BiI_3 are higher than that of q-1D BiI_3, indicating that the higher generalized group velocity results in the weaker phonon localization, potentially leading to a higher coherent thermal conductivity.

Based on the analysis of mode diffusivity, we further study the coherent-mode-dependent contributions to the coherent thermal conductivity at 300 K for correlating the V_{ij}^2 with κ_L^C. The heat maps in Figs. 3(d)–3(f) show the contributions of coherent phonon modes in different frequency regions to the total κ_L^C. It is noteworthy that the contribution from coherent modes to the coherent thermal conductivity in the z direction of q-1D BiI_3 is similar to that in the x direction of q-1D TiS_3 within a comparable frequency range of 4 THz, as verified by the calculated values of κ_L^C shown in Fig. 2(a). However, the situation is different for the x direction of q-1D BiI_3, where the contributions are small in the entire frequency range. Meanwhile, we found that when $\Delta\omega/2\pi < 0.5$ THz as indicated by the dashed lines in Fig. 3, the distribution of coherent-mode-dependent contributions to κ_L^C shows a clear correlation with the distribution of projected V_{ij}^2, further confirming the correlation analysis discussed above.

Overall, when considering coherent phonon modes that contribute significantly to κ_L^C, the correlation between their V_{ij}^2

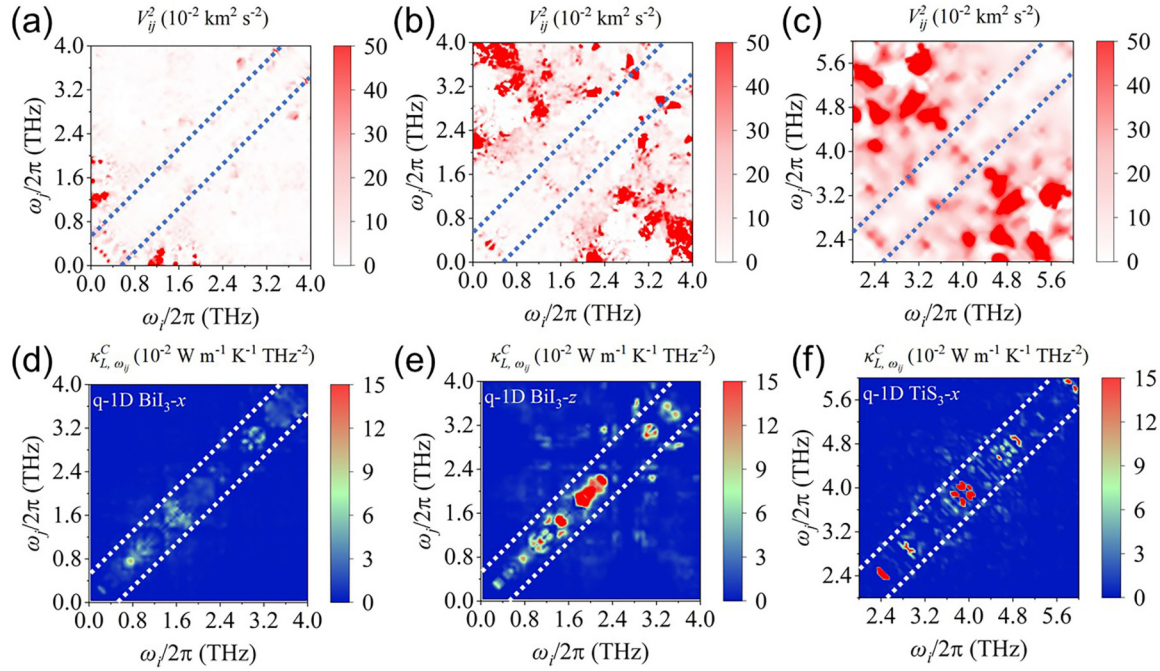

FIG. 3. Numerical correlation between the generalized group velocity and coherent thermal conductivity. (a)−(c) Projection of the square of the generalized group velocity (V_{ij}^2), (d)−(f) corresponding coherent-mode-dependent contributions to the κ_L^C vs coherent phonon frequencies at 300 K. The color bars represent the absolute values of the plotted data. Dashed lines refer to where the $\Delta\omega/2\pi = 0.5$ THz, clarifying the correlation between the V_{ij}^2 and κ_L^C.

and κ_L^C is relatively strong, which reveals that the magnitude of the V_{ij}^2 has a significant influence on the coherent thermal conductivity in these crystals. Thus V_{ij}^2 could serve as a primary parameter in searching for the crystals with extremely low two-channel thermal conductivity. This conclusion is also confirmed by comparing the V_{ij}^2 and the coherent-mode-dependent contributions in different directions of $R-3$ BiI_3 (see Fig. S13 in the SM [28]).

D. Generalized coherent lifetime and average mode frequency interval

To provide the evidence for the significant influence of the generalized coherent lifetime (τ_{ij}) and frequency interval of coherent phonon modes ($\Delta\omega$) on the coherent lattice thermal conductivity, we plot the distribution of τ_{ij} in the coherent lifetime space for q-1D BiI_3, $R-3$ BiI_3, and q-1D TiS_3 in Figs. 4(a)–4(c), which show that for the two q-1D structures, the overall distribution of τ_{ij} is relatively far from the peak values in the coherent lifetime space, as indicated by the yellow dashed lines. This can be attributed to the relatively moderate $\Delta\omega$ in the two structures, while the τ_{ij} of $R-3$ BiI_3 is more concentrated around the extremum, exhibiting higher absolute values. Based on this comparison, one can see that the coherent phonon modes with larger $\Delta\omega$ exhibit smaller τ_{ij}, thereby suppressing the κ_L^C. To establish a better understanding of this phenomenon, we further analyze the relationship between the lifetime of individual phonon modes (τ_i) in these systems and their contributions to thermal conductivity. Here, N_{at} is the number of atoms per unit cell, $1/\Delta\omega_{\text{ave}} = 3N_{\text{at}}/\omega_{\max}$ is a criterion for determining the boundary of phonon coherence contributions, also known as the Wigner limit in time. Phonon modes with τ_i below this limit mainly contribute to coherent thermal conductivity, and the Ioffe-Regel limit ($1/\omega$) [50] can be used to assess whether the assumption of phonon quasiparticle excitations is valid. When the τ_i of a large amount of phonon modes is below the Ioffe-Regel limit, the phonons are in an overdamped state, where the consideration of phonon spectral functions is required [51,52]. Our analysis reveals that all the studied systems fully follow the Wigner framework. Furthermore, the distribution of τ_i in q-1D BiI_3 is mainly around the Wigner limit in time, and the lower τ_i also suppresses the lattice thermal conductivity contributed from the particlelike propagation.

In addition, according to Eq. (5),

$$\frac{\kappa^C_{L,\text{ave}}(\mathbf{q})_i}{\kappa^P_{L,\text{ave}}(\mathbf{q})_i} \simeq \frac{\Delta\omega_{\text{ave}}}{\Gamma(\mathbf{q})_i} = \frac{\tau(\mathbf{q})_i}{1/\Delta\omega_{\text{ave}}}, \tag{5}$$

the contributions of phonon modes to κ_L^P and κ_L^C in q-1D BiI_3 are proportionate, which is consistent with the calculated result shown in the pie chart in Fig. 4(d). In contrast, due to the extremely low $1/\Delta\omega_{\text{ave}}$, most phonon modes in q-1D TiS_3 primarily contribute to the particlelike propagation primarily by the acoustic phonons, as presented in Fig. 4(f). Moreover, the numerous phonon modes generated by the 24 atoms in the unit cell of $R-3$ BiI_3 result in a higher Wigner limit in time. Therefore, despite having the higher τ_i and κ_L^P, compared to those of q-1D BiI_3, $R-3$ BiI_3 exhibits an even higher proportion of coherent thermal conductivity, as illustrated in Fig. 4(e).

Overall, the extremely low phonon frequency distribution ($\omega_{\max}/2\pi = 4.05$ THz) of q-1D BiI_3 results in the ultralow

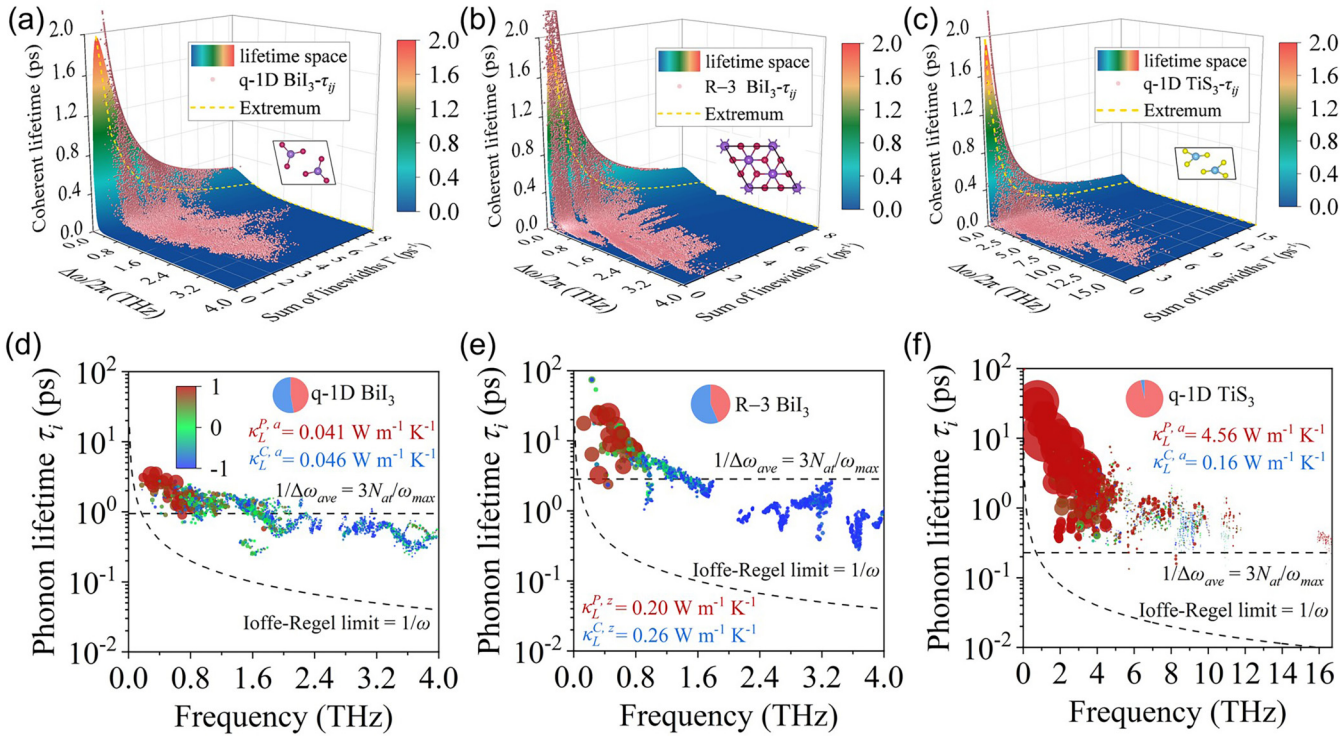

FIG. 4. Characterization of the lifetime for phonons and their coherent modes. (a)–(c) Distribution of the generalized coherent lifetime τ_{ij}. The yellow dashed lines represent the extremum value of τ_{ij} at the same $\Delta\omega/2\pi$. (d)–(f) Variation of the single phonon modes lifetime τ_i with phonon frequency at 300 K. The black dashed lines and dashed curves are for the Wigner time limit ($1/\Delta\omega_{\text{ave}}$) and Ioffe-Regel limit ($1/\omega$), respectively. The areas of the circles represent the proportion of the contribution to the total thermal conductivity: red for particlelike propagation and blue for phonon coherence, and green in color bars corresponds to an equal contribution from both transport mechanisms. The insert pie charts show the proportions of particlelike and coherence thermal conductivity.

V_{ij} coupled with strong anharmonicity. Meanwhile, the moderate $\Delta\omega$ determined by the simple crystal structure reduces the Wigner limit in time, effectively suppressing the ratio of κ_L^C/κ_L^P to near 1, which leads to an ultralow total lattice thermal conductivity. In addition to the detailed analysis, we also need to provide a brief description of the underlying physical picture to support our conclusions discussed above.

E. Strategies for designing materials with ultralow lattice thermal conductivity

From Figs. 4(d)–4(f), one can see that the κ_L^P values in all the three structures are primarily contributed from their acoustic phonons and a small portion of extremely low-frequency optical phonons. This is consistent with previous studies that refer to the phonon modes below the Ioffe-Regel critical frequency (ω_{IR}) as propagons, and those above as diffusons and locons [53,54], indicating that the modes below the ω_{IR} primarily contribute to κ_L^P, while those above the value mainly contribute to κ_L^C. One can see that the diffusons are mainly consist of optical phonons. This is because the optical phonons are more localized than the acoustic phonons but still carry a significant portion of thermal energy for propagating coherently between different modes. To clarify the capacity of thermal carriers, we plot the isochoric lattice heat capacity

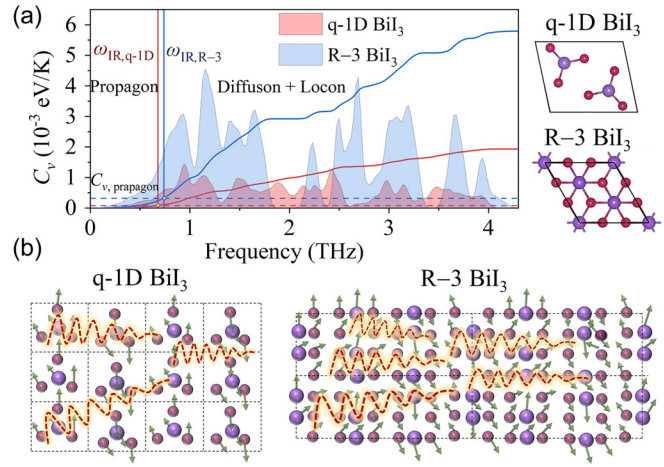

FIG. 5. Mechanism of suppressing diffusons. (a) Isochoric lattice heat capacity (C_v), where the vertical lines represent ω_{IR} and the horizontal lines correspond to the heat capacity values contributed by propagons. The shaded area represents the derivative of heat capacity with respect to frequency. (b) Schematic diagram illustrating the difference between the simple (q-1D BiI_3) and complex (R−3 BiI_3) structures in thermal conductivity: the complex lattice producing more optical phonons for coherence thermal conductivity. The green arrows reflect the complexity of the atomic vibrations.

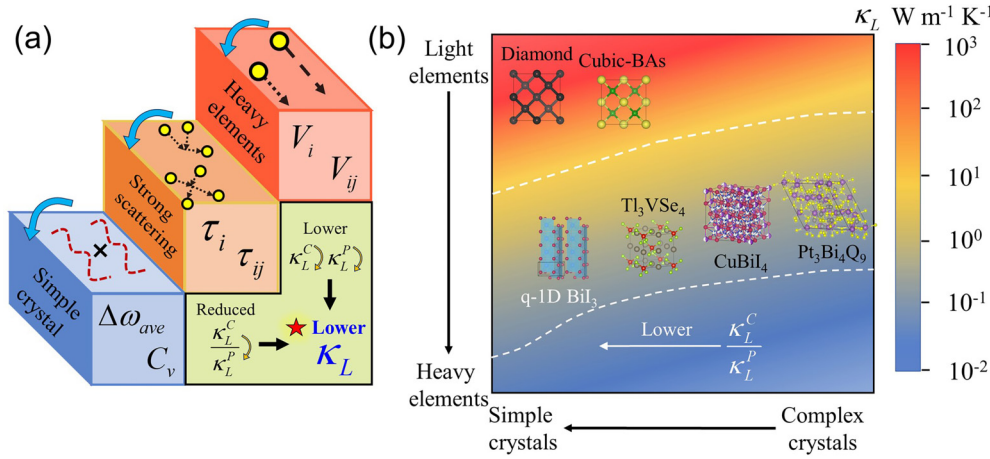

FIG. 6. Schematic diagram of the physical mechanism for designing materials with ultralow lattice thermal conductivity. (a) Key properties and physical parameters for achieving ultralow lattice thermal conductivity (κ_L), and (b) lattice thermal conductivity changing with elements and geometry, where the dashed lines represent the values of 10^2 and 10^{-1} W m^{-1} K^{-1}, respectively.

(C_v) of q-1D BiI_3 and $R-3$ BiI_3 in Fig. 5(a), showing that $R-3$ BiI_3 with a larger number of atoms in its unit cell has a higher lattice heat capacity, but the contribution from its propagons is similar to that for q-1D BiI_3. Moreover, one can see from Fig. 2(c) that the correlation between the heat capacity of coherent phonon modes and κ_L^C is weak. Therefore, the relatively independent isochoric heat capacity determines the energy-carrying capacity of different phonon modes, affecting the ratio of κ_L^C dominated by diffusons to κ_L^P dominated by propagons; Fig. 5(b) schematically illustrates the origin of lower κ_L^C in crystals with small number of atoms in the unit cell.

Based on above discussion, we elaborate on the physical mechanism of the strategy for designing materials with ultralow thermal conductivity: simple and strongly anharmonic crystals containing heavy elements for achieving ultralow lattice thermal conductivity by synergistically suppressing the particlelike propagation and wavelike tunneling. As illustrated in Fig. 6(a), heavy elements and strong anharmonicity suppress the group velocity (V_i, V_{ij}) and lifetime (τ_i, τ_{ij}) of phonons and their coherent modes in crystals, leading to low κ_L^P and κ_L^C, while the simple geometric structures with a small number of atoms limit the wavelike tunneling, because the number of diffusons is limited by the number of atoms in the unit cell due to the less optical phonons in simple crystals, resulting in low ratio of κ_L^C/κ_L^P. Thus, the synergistic coupling of these two mechanisms results in ultralow thermal conductivity. For instance, the lattice thermal conductivities of Tl_3VSe_4 [8], $CuBiI_4$ [55], and $Pt_3Bi_4Q_9$ ($Q =$ S, Se) [13] composed of heavy elements with strong anharmonicity are about 0.30, 0.34, and 0.59 W m^{-1} K^{-1}, respectively, which are much lower than those of harmonic lightweight materials, such as diamond (~2000 W m^{-1} K^{-1}) [56] and cubic boron arsenide (~1310 W m^{-1} K^{-1}) [57]. However, their average lattice thermal conductivities are still higher than that of q-1D BiI_3 due to the more complex structures [Fig. 6(b)] with 16 [8], 48 [55], and 96 atoms [13] in their unit cells. Accordingly, their phonon coherence makes more contribution to thermal transport compared to that in q-1D BiI_3. This in-depth understanding would effectively promote the discovery of crystals with ultralow thermal conductivity.

IV. CONCLUSIONS

In summary, this work focuses on an important question: how to design new crystal structures with strong anharmonicity and weak phonon coherence to achieve ultralow lattice thermal conductivity. Using a structure search, a different bulk phase of quasi-one-dimensional crystal, q-1D BiI_3 composed of BiI_3 chains, is found. Compared with the well-known layered $R-3$ BiI_3 phase, this chainlike BiI_3 phase has enhanced anharmonicity but with much less atoms in its unit cell (8 vs 24 atoms). Based on the Wigner thermal transport theory and MD simulations with machine learning potential, we have found that q-1D BiI_3 possesses an ultralow lattice thermal conductivity of 0.088 (0.099) W m^{-1} K^{-1} in the $x(y)$ direction within the Wigner framework. Through correlation analysis, we further identified that the generalized group velocity (V_{ij}), the frequency interval ($\Delta\omega$), and the generalized coherent lifetime (τ_{ij}) are the main factors affecting the coherent thermal conductivity. Especially, the fewer atoms in the unit cell of this new phase reduces the number of diffusons for coherence thermal transport. Therefore, the reduced phonon coherence, together with the enhanced strong anharmonicity due to the unique geometry with weakly coupled chains, make the new phase of BiI_3 exhibit an ultralow lattice thermal conductivity. This work provides insight into the complex correlations among the physical quantities that are closely related to lattice thermal conductivity for guiding the design of materials with ultralow thermal conductivity.

ACKNOWLEDGMENTS

This work was supported by grants from the National Natural Science Foundation of China (Grant No. NSFC-12274007), and is also supported by the High-Performance Computing Platform of Peking University, China.

[1] X. Qian, J. Zhou, and G. Chen, Phonon-engineered extreme thermal conductivity materials, Nat. Mater. **20**, 1188 (2021).

[2] R. Zhang, L. Gan, D. Zhang, H. Sun, Y. Li, and C. Z. Ning, Extreme thermal insulation and tradeoff of thermal transport mechanisms between graphene and WS_2 monolayers, Adv. Mater. **36**, 2313753 (2024).

[3] M. Omini and A. Sparavigna, An iterative approach to the phonon Boltzmann equation in the theory of thermal conductivity, Physica B: Condens. Matter **212**, 101 (1995).

[4] G. A. Slack, Nonmetallic crystals with high thermal conductivity, J. Phys. Chem. Solids **34**, 321 (1973).

[5] Q. D. Gibson, T. Zhao, L. M. Daniels, H. C. Walker, R. Daou, S. Hébert, M. Zanella, M. S. Dyer, J. B. Claridge, and B. Slater, Low thermal conductivity in a modular inorganic material with bonding anisotropy and mismatch, Science **373**, 1017 (2021).

[6] Z. Tong, A. Pecchia, C. Yam, T. Dumitrică, and T. Frauenheim, Glass-like transport dominates ultralow lattice thermal conductivity in modular crystalline $Bi_4O_4SeCl_2$, Nano Lett. **23**, 9468 (2023).

[7] Q. Ren, M. K. Gupta, M. Jin, J. Ding, J. Wu, Z. Chen, S. Lin, O. Fabelo, J. A. Rodríguez-Velamazán, M. Kofu *et al.*, Extreme phonon anharmonicity underpins superionic diffusion and ultralow thermal conductivity in argyrodite Ag_8SnSe_6, Nat. Mater. **22**, 999 (2023).

[8] S. Mukhopadhyay, D. S. Parker, B. C. Sales, A. A. Puretzky, M. A. McGuire, and L. Lindsay, Two-channel model for ultralow thermal conductivity of crystalline Tl_3VSe_4, Science **360**, 1455 (2018).

[9] M. Simoncelli, N. Marzari, and F. Mauri, Unified theory of thermal transport in crystals and glasses, Nat. Phys. **15**, 809 (2019).

[10] M. Simoncelli, N. Marzari, and F. Mauri, Wigner formulation of thermal transport in solids, Phys. Rev. X **12**, 041011 (2022).

[11] T. Li, P.-H. Du, L. Bai, Q. Sun, and P. Jena, Thermoelectric figure of merit of a superatomic crystal $Re_6Se_8I_2$ monolayer, Phys. Rev. Appl. **18**, 064067 (2022).

[12] P.-H. Du, C. Zhang, T. Li, and Q. Sun, Low lattice thermal conductivity with two-channel thermal transport in the superatomic crystal PH_4AlBr_4, Phys. Rev. B **107**, 155204 (2023).

[13] R. Wang, F. Liang, X. Zhang, C. Zhao, Y. Fang, C. Zheng, and F. Huang, Ultralow thermal conductivity of a chalcogenide system $Pt_3Bi_4Q_9$ (Q = S, Se) driven by the hierarchy of rigid $[Pt_6Q_{12}]^{12-}$ clusters embedded in soft Bi-Q sublattice, J. Am. Chem. Soc. **146**, 7352 (2024).

[14] Z. Zeng, X. Shen, R. Cheng, O. Perez, N. Ouyang, Z. Fan, P. Lemoine, B. Raveau, E. Guilmeau, and Y. Chen, Pushing thermal conductivity to its lower limit in crystals with simple structures, Nat. Commun. **15**, 3007 (2024).

[15] C. Chiritescu, D. G. Cahill, N. Nguyen, D. Johnson, A. Bodapati, P. Keblinski, and P. Zschack, Ultralow thermal conductivity in disordered, layered WSe_2 crystals, Science **315**, 351 (2007).

[16] A. Lipatov, M. J. Loes, H. Lu, J. Dai, P. Patoka, N. S. Vorobeva, D. S. Muratov, G. Ulrich, B. Kästner, and A. Hoehl, Quasi-1D TiS_3 nanoribbons: Mechanical exfoliation and thickness-dependent Raman spectroscopy, ACS Nano **12**, 12713 (2018).

[17] C. Liu, C. Wu, X. Y. Tan, Y. Tao, Y. Zhang, D. Li, J. Yang, Q. Yan, and Y. Chen, Unexpected doping effects on phonon transport in quasi-one-dimensional van der Waals crystal TiS_3 nanoribbons, Nat. Commun. **14**, 5597 (2023).

[18] M. Chen, L. Li, M. Xu, W. Li, L. Zheng, and X. Wang, Quasi-one-dimensional van der Waals transition metal trichalcogenides, Research **6**, 0066 (2023).

[19] Z. Fan, Improving the accuracy of the neuroevolution machine learning potential for multi-component systems, J. Phys.: Condens. Matter **34**, 125902 (2022).

[20] P. E. Blöchl, Projector augmented-wave method, Phys. Rev. B **50**, 17953 (1994).

[21] G. Kresse and D. Joubert, From ultrasoft pseudopotentials to the projector augmented-wave method, Phys. Rev. B **59**, 1758 (1999).

[22] G. Kresse and J. Furthmüller, Efficient iterative schemes for ab initio total-energy calculations using a plane-wave basis set, Phys. Rev. B **54**, 11169 (1996).

[23] J. P. Perdew, K. Burke, and M. Ernzerhof, Generalized gradient approximation made simple, Phys. Rev. Lett. **77**, 3865 (1996).

[24] Y. Hu and C. Storey, Efficient generalized conjugate gradient algorithms, part 2: Implementation, J. Optim. Theory Appl. **69**, 139 (1991).

[25] S. Grimme, J. Antony, S. Ehrlich, and H. Krieg, A consistent and accurate *ab initio* parametrization of density functional dispersion correction (DFT-D) for the 94 elements H-Pu, J. Chem. Phys. **132**, 154104 (2010).

[26] H. J. Monkhorst and J. D. Pack, Special points for Brillouin-zone integrations, Phys. Rev. B **13**, 5188 (1976).

[27] Z. Han, X. Yang, W. Li, T. Feng, and X. Ruan, FourPhonon: An extension module to ShengBTE for computing four-phonon scattering rates and thermal conductivity, Comput. Phys. Commun. **270**, 108179 (2022).

[28] See Supplemental Material at http://link.aps.org/supplemental/10.1103/PhysRevB.110.174309 for additional information about the computational methods, supplemental figures and tables of simulations, which includes Refs. [29,30].

[29] H. Gao, J. Wang, Y. Han, and J. Sun, Enhancing crystal structure prediction by decomposition and evolution schemes based on graph theory, Fundam. Res. **1**, 466 (2021).

[30] F. Mouhat and F.-X. Coudert, Necessary and sufficient elastic stability conditions in various crystal systems, Phys. Rev. B **90**, 224104 (2014).

[31] A. Togo and I. Tanaka, First principles phonon calculations in materials science, Scr. Mater. **108**, 1 (2015).

[32] F. Eriksson, E. Fransson, and P. Erhart, The Hiphive Package for the extraction of high-order force constants by machine learning, Adv. Theory. Simul. **2**, 1800184 (2019).

[33] E. Fransson, F. Eriksson, and P. Erhart, Efficient construction of linear models in materials modeling and applications to force constant expansions, npj Comput. Mater. **6**, 135 (2020).

[34] Z. Fan, H. Dong, A. Harju, and T. Ala-Nissila, Homogeneous nonequilibrium molecular dynamics method for heat transport and spectral decomposition with many-body potentials, Phys. Rev. B **99**, 064308 (2019).

[35] Z. Fan, Y. Wang, P. Ying, K. Song, J. Wang, Y. Wang, Z. Zeng, K. Xu, E. Lindgren, J. M. Rahm *et al.*, GPUMD: A package for constructing accurate machine-learned potentials and performing highly efficient atomistic simulations, J. Chem. Phys. **157**, 114801 (2022).

[36] U. Schwarz, A. Wosylus, M. Schmidt, L. Akselrud, A. Ormeci, M. Hanfland, V. Hermann, and C. Kuntscher, High-pressure modification of BiI_3, Inorganics **7**, 143 (2019).

[37] X. Wang, J. Wu, J. Wang, T. Chen, H. Gao, P. Lu, Q. Chen, C. Ding, J. Wen, and J. Sun, Pressure-induced structural and electronic transitions in bismuth iodide, Phys. Rev. B **98**, 174112 (2018).

[38] K. Xia, H. Gao, C. Liu, J. Yuan, J. Sun, H.-T. Wang, and D. Xing, A novel superhard tungsten nitride predicted by machine-learning accelerated crystal structure search, Sci. Bull. **63**, 817 (2018).

[39] J. Wang, H. Gao, Y. Han, C. Ding, S. Pan, Y. Wang, Q. Jia, H.-T. Wang, D. Xing, and J. Sun, MAGUS: Machine learning and graph theory assisted universal structure searcher, Natl. Sci. Rev. **10**, nwad128 (2023).

[40] I. S. Novikov, K. Gubaev, E. V. Podryabinkin, and A. V. Shapeev, The MLIP package: Moment tensor potentials with MPI and active learning, Mach. Learn.: Sci. Technol. **2**, 025002 (2021).

[41] A. Jain, S. P. Ong, G. Hautier, W. Chen, W. D. Richards, S. Dacek, S. Cholia, D. Gunter, D. Skinner, G. Ceder, and K. A. Persson, Commentary: The Materials Project: A materials genome approach to accelerating materials innovation, APL Mater. **1**, 011002 (2013).

[42] J. Trotter and T. Zobel, The crystal structure of SbI_3 and BiI_3, Z. Kristallogr.-Cryst. Mater. **123**, 67 (1966).

[43] M. Born, K. Huang, and M. Lax, Dynamical theory of crystal lattices, Am. J. Phys. **23**, 474 (1955).

[44] T. Feng and X. Ruan, Quantum mechanical prediction of four-phonon scattering rates and reduced thermal conductivity of solids, Phys. Rev. B **93**, 045202 (2016).

[45] Y. Chen, C. Zhang, J. Sun, D. Ni, C. Zhang, and Q. Wang, Tuning the lattice thermal conductivity of bilayer penta-graphene by interlayer twisting, Appl. Surf. Sci. **635**, 157718 (2023).

[46] C. Zhang, J. Sun, Y. Shen, C. Zhang, Q. Wang, A. Yoshikawa, Y. Kawazoe, and P. Jena, Extremely large response of phonon coherence in twisted penta-NiN_2 bilayer, Small **19**, 2303295 (2023).

[47] P. B. Allen and J. L. Feldman, Thermal conductivity of disordered harmonic solids, Phys. Rev. B **48**, 12581 (1993).

[48] A. Auerbach and P. B. Allen, Universal high-temperature saturation in phonon and electron transport, Phys. Rev. B **29**, 2884 (1984).

[49] Y. Luo, X. Yang, T. Feng, J. Wang, and X. Ruan, Vibrational hierarchy leads to dual-phonon transport in low thermal conductivity crystals, Nat. Commun. **11**, 2554 (2020).

[50] A. Ioffe and A. Regel, Non-crystalline, amorphous, and liquid electronic semiconductors, Prog. Semicond. **4**, 237 (1960).

[51] P. Sheng, M. Zhou, and Z.-Q. Zhang, Phonon transport in strong-scattering media, Phys. Rev. Lett. **72**, 234 (1994).

[52] G. Caldarelli, M. Simoncelli, N. Marzari, F. Mauri, and L. Benfatto, Many-body Green's function approach to lattice thermal transport, Phys. Rev. B **106**, 024312 (2022).

[53] Y. M. Beltukov, C. Fusco, D. A. Parshin, and A. Tanguy, Boson peak and Ioffe-Regel criterion in amorphous siliconlike materials: The effect of bond directionality, Phys. Rev. E **93**, 023006 (2016).

[54] Y. M. Beltukov, D. A. Parshin, V. M. Giordano, and A. Tanguy, Propagative and diffusive regimes of acoustic damping in bulk amorphous material, Phys. Rev. E **98**, 023005 (2018).

[55] A. Das, K. Pal, P. Acharyya, S. Das, K. Maji, and K. Biswas, Strong antibonding I (p)–Cu (d) states lead to intrinsically low thermal conductivity in CuBiI4, J. Am. Chem. Soc. **145**, 1349 (2023).

[56] L. Wei, P. K. Kuo, R. L. Thomas, T. R. Anthony, and W. F. Banholzer, Thermal conductivity of isotopically modified single crystal diamond, Phys. Rev. Lett. **70**, 3764 (1993).

[57] F. Tian, B. Song, X. Chen, N. K. Ravichandran, Y. Lv, K. Chen, S. Sullivan, J. Kim, Y. Zhou, and T.-H. Liu, Unusual high thermal conductivity in boron arsenide bulk crystals, Science **361**, 582 (2018).